Real-time reconstruction of unsteady rotating forces acting by rotor blades in moving medium

Xu, Ying; Casalino, Damiano; Zhang, Xiao Zheng; Zhang, Yong Bin; Bi, Chuan Xing

DOI
10.1016/j.jsv.2023.117972

Publication date
2024

Document Version
Final published version

Published in
Journal of Sound and Vibration

Journal of Sound and Vibration 568 (2024) 117972

Contents lists available at ScienceDirect

Journal of Sound and Vibration

journal homepage: www.elsevier.com/locate/jsvi

Real-time reconstruction of unsteady rotating forces acting by rotor blades in moving medium

Ying Xu [a], Damiano Casalino [b], Xiao-Zheng Zhang [a], Yong-Bin Zhang [a], Chuan-Xing Bi [a,*]

[a] Institute of Sound and Vibration Research, Hefei University of Technology, 193 Tunxi Road, Hefei 230009, People's Republic of China
[b] Flow Physics and Technology Department, Delft University of Technology, Kluyverweg 1, Delft 2629HS, the Netherlands

ARTICLE INFO

Keywords:
Rotor noise
Unsteady rotating forces
Moving medium
Real-time reconstruction
Inverse aeroacoustic method

ABSTRACT

A time-domain inverse aeroacoustic method based on the convective Ffowcs Williams–Hawkings equation is presented. The method allows to determine, in real-time, the unsteady forces exerted on rotating blades in the presence of a moving medium. The inversion procedure is based on a space-time regularization with a mixed $l_{1,2}$-norm, which guarantees accuracy and smoothness of the solution. The method is initially verified through synthetic acoustic signals emitted by rotating sources in a constant flow, up to a convective Mach number of about 0.88. Then the method is validated through signals generated by a propeller immersed in a wind-tunnel jet flow, up to a Mach number of 0.06. Due to the reduced convective Mach number, the leading aeroacoustic effect is derived from a variation of the blade loading. It is argued that the onset of flow separation at high values of the rotor advance ratio is responsible for the onset of force fluctuations that the inverse method is able to retrieve both qualitatively and quantitatively.

1. Introduction

With the rapid development of advanced air mobility concepts based on electric Vertical Take-Off and Landing (eVTOL) vehicles, lifted and propelled by multiple distributed rotors, modeling and measurements of rotating aeroacoustic sources have become a topic of high scientific and technical relevance. Among other design challenges [1], a low noise signature is crucial for the societal acceptance of operations in closer proximity of highly densely populated [2,3].

The theory of sound generation from rotors is based on the acoustic analogy for arbitrarily moving surfaces formulated by Ffowcs-Williams and Hawkings [4]. The engineering relevance of the theory is instead related to the mathematical derivations by Farassat and Succi [5], and the computational algorithms proposed by several authors [6–9]. This literature is related to the challenge of predicting rotorcraft noise in a broad range of Mach numbers. More recently, due to the emergence of drone and eVTOL aeroacoustics, researchers have faced new challenges related to transitional nature of the flow [10–12], to the unsteady nature of the forces applied on the rotor blades in non-axial flow conditions [13] and in the presence of inflow turbulence [14], and to the stochastic variation of the rotational speed [15]. The unsteady loading effects, in particular, are crucial for reliable community noise assessments, since the acoustic annoyance is strongly related to the occurrence of amplitude and frequency modulations. These effects are relevant in hover conditions, when the controller continuously adapts the Revolutions Per Minute (RPM) of every rotor to keep the hovering point, as well as

* Corresponding author.
E-mail address: cxbi@hfut.edu.cn (C.-X. Bi).

https://doi.org/10.1016/j.jsv.2023.117972
Received 23 March 2023; Received in revised form 9 July 2023; Accepted 30 July 2023
Available online 31 July 2023

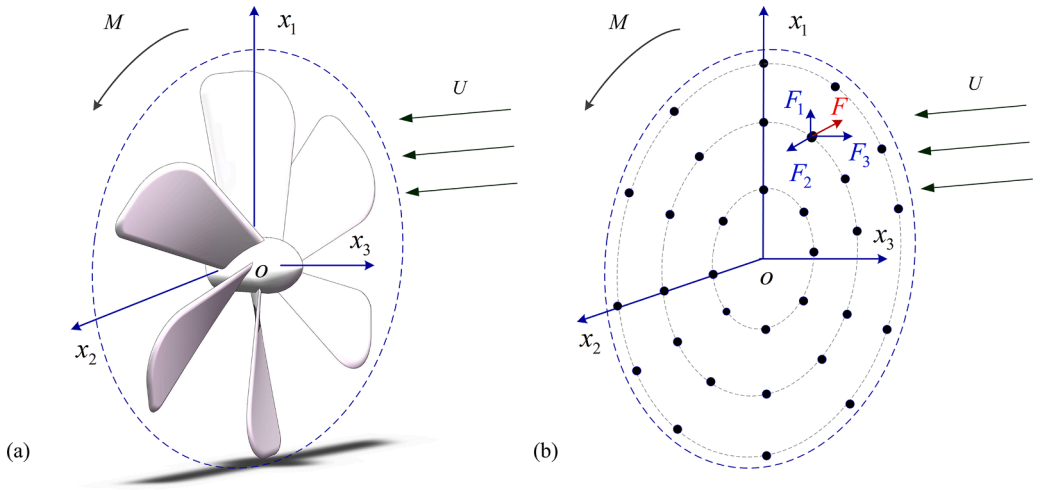

Fig. 1. Geometric description of the rotor planform (a) and the equivalent discrete source points (b). *M* and *U* are the rotational (tip) Mach number and the moving flow velocity, respectively.

during maneuvers, when the rotors operate in non-axial flow conditions, or blade-vortex interaction phenomena may occur, or the RPM is changed abruptly. To shed light on these effects, the time evolution of the blade loading should be scrutinized both experimentally and numerically. The present work contributes to the development of an inverse acoustic method for the experimental characterization of unsteady blade loading, and in particular it is focused on the inclusion of mean-flow convective effects in the formulation of the inverse problem.

In the past decades, acoustic imaging methods based on microphone array measurements [16], such as beamforming methods [17,18], inverse methods [19,20] and nearfield acoustic holography methods [21,22], have been widely used to identify the aeroacoustic sources in moving medium. These methods were originally proposed for static aeroacoustic sources. For rotating aeroacoustic sources, such as propeller noise [23], the sound field is much more complicated than the sound field of static sources due to the Doppler effect [24]. The identification methods for the static aeroacoustic sources are usually not suitable for the identification of rotating aeroacoustic sources [25]. At present, many methods have been proposed to perform rotating aeroacoustic source identification [26–29], such as the classic de-Doppler techniques [30], virtual rotating array method [31] and mode decomposition methods [32]. However, these methods are usually based on the static/quiescent medium assumption.

To identify rotating aeroacoustic sources in a uniform subsonic axial flow, Sijtsma [33,34] first developed the 'rotating source identifier' method based on the assumption of monopole sources in time domain by considering motion compensation, which was successfully applied to locate and estimate propeller noise in the open jet of the German-Dutch Wind Tunnels using an out-of-flow acoustic array. Then, Ocker and Pannert [35] developed a frequency domain method for locating rotating monopole sources in axial flow by considering motion compensation and a uniform subsonic axial flow. The method utilizes a modified free-space Green's function in the virtual rotating array to describe the rotating sound field analytically. To further improve the location resolution of rotor blade noise, Yu et al. [36] introduced a cyclostationary signal processing tool into the beamforming method to extract the rotor blade signals from the noisy measurements with other interferences. However, this method is still based on the assumption of monopole sources. It is worth noting that in subsonic flows, the loading noise is related to a dipole source due to the unsteady forces exerted by the solid surfaces on the fluid and it is the principal cause of propeller noise in most aeroacoustic systems [37,38]. For identifying rotating loading sources in moving medium, Chen et al. [39] proposed a wavelet-based beamforming method in the time-frequency domain and carried out experimental researches with a rotating blade and the airfoil in an anechoic wind tunnel. Unfortunately, the beamforming methods failed to quantify the source strengths accurately when multiple coherent sources were present. To evaluate the unsteady rotating forces exerted by the rotor blades on the surrounding fluid, Gerard et al. [40] investigated an inverse acoustic method based on the Helmholtz integral solution following the approach of Morse and Ingard. Later on, Trabelsi et al. [41] developed an inverse method to evaluate the unsteady rotating forces applied by fan blades on the surrounding fluid, but they employed a simple model of the tonal noise of an axial flow fan, in which the distributed force was replaced by an equivalent force concentrated at the aerodynamic center of the blade.

The existing researches on the reconstruction of the unsteady rotating forces in moving medium by the inverse method were carried out in the frequency domain, thus losing some information about the variation of the sources in time. This information is indeed key for real-time identification and control of moving sources and it is of scientific significance and practical importance. Therefore, in the present paper, a time-domain inverse aeroacoustic method is established based on the convective Ffowcs Williams–Hawkings (FW-H) equation. To validate the model, experiments are performed by locating the rotor of an unmanned aerial vehicle (UAV) in the flow issued at different velocity by a nozzle located in a semi-anechoic open wind tunnel in Hefei University of Technology. The measured signals are used to carry out a real-time reconstruction of the unsteady forces acting on the rotor blades, by taking into account the small but not negligible acoustic convective effects of the mean flow.

The remainder of the present paper is organized as follows. Section 2 presents the theoretical formulations of the proposed time-domain inverse aeroacoustic method. In Section 3, synthetic noise signals radiated by two unsteady rotating point forces in a uniform flow are computed analytically and used as an input of the proposed method to systematically evaluate its accuracy. In Section 4, experimental noise signals emitted by an UAV rotor in an open wind tunnel are used to validate the proposed method in a more realistic operational scenario. Finally, the main outcome and conclusions of the present work are drawn in Section 5.

2. Theoretical formulations

2.1. The time-domain inverse aeroacoustic method

According to the aeroacoustic theories of rotors, steady and unsteady forces generated by the flow on the blades are the dominant sources of thin blades in subsonic, low Mach number conditions. Therefore, the proposed inverse method should seek for dipole sources distrusted on the rotor disk [42], which is discretized into N loading source points in a moving medium, marked by solid circles, as shown in Fig. 1. The force at each source point is decomposed into the three components in the Cartesian coordinate system. The model derivation starts from the equations of sound pressure at a given microphone location $\mathbf{x}$ and time t generated by these N loading sources in a moving medium. By using the retarded time formulation 1C based on the convective wave equation, which takes into account the presence of a mean flow [43], the pressure signal reads:

$$\begin{aligned} p(\mathbf{x},t) = & \frac{1}{4\pi c}\sum_{n=1}^{N}\left[\frac{\dot{F}_i\widetilde{R}_i}{R^*(1-M_i\widetilde{R}_i)^2}\right]_e + \frac{1}{4\pi}\sum_{n=1}^{N}\left[\frac{F_i\widetilde{R}_i^* - F_iM_i}{R^{*2}(1-M_i\widetilde{R}_i)^2}\right]_e \\ & + \frac{1}{4\pi c}\sum_{n=1}^{N}\left[F_i\widetilde{R}_i\frac{R^*\dot{M}_i\widetilde{R}_i + c_0\left(M_i\widetilde{R}_i^* - M^2\right)}{R^{*2}(1-M_i\widetilde{R}_i)^3}\right]_e \\ & - \frac{1}{4\pi}\sum_{n=1}^{N}\left[F_i\widetilde{R}_i\frac{M_i\widetilde{R}_i^*M_i\widetilde{R}_i + \gamma^2\left((M_{\infty i}M_i)^2 - \left(M_i\widetilde{R}_i^*\right)^2\right)}{R^{*2}(1-M_i\widetilde{R}_i)^3}\right]_e, \\ & - \frac{1}{4\pi}\sum_{n=1}^{N}\left[\frac{F_i\widetilde{R}_i^*M_i\widetilde{R}_i + \gamma^2\left(M_{\infty i}M_iM_{\infty i}F_i - F_i\widetilde{R}_i^*M_i\widetilde{R}_i^*\right)}{R^{*2}(1-M_i\widetilde{R}_i)^2}\right]_e \end{aligned} \tag{1}$$

where the subscript "n" indicates the nth source point; $\dot{F}_{ni}$ is the derivative of the force component of the nth source F_{ni} with respect to the source time, i.e., $\dot{F}_{ni} = \partial F_{ni}/\partial\tau$; M_{ni} is the Mach number component of the nth source, with $M_{ni} = V_{ni}/c$ where V_{ni} is the velocity component of the nth source; M_n is the Mach number of the nth source; $\dot{M}_{ni}$ is the derivative of M_{ni} in terms of the source time, i.e., $\dot{M}_{ni} = \partial M_{ni}/\partial\tau$; M_∞ is the amplitude of the flow Mach number vector $\mathbf{M}_\infty$; $M_{\infty i}$ is the component of the flow Mach number, with $M_{\infty i} = U_i/c$ where U_i is the velocity component of the moving flow velocity U; r is the amplitude of the distance vector $\mathbf{r}$; The subscript "e" in Eq. (1) indicates that all the quantities in the square brackets depend on their evaluated values at the source time τ. Other quantities are defined as:

$$R^* = \frac{1}{\gamma}\sqrt{r^2 + \gamma^2(\mathbf{M}_\infty\cdot\mathbf{r})^2}, \tag{2}$$

$$R = \gamma^2(R^* - \mathbf{M}_\infty\cdot\mathbf{r}), \tag{3}$$

$$\gamma^2 = 1\Big/\left(1 - |\mathbf{M}_\infty|^2\right), \tag{4}$$

$$\widetilde{R}_i^* = \frac{\partial R^*}{\partial x_i} = \frac{r_i + \gamma^2\left(M_{\infty j}r_j\right)M_{\infty i}}{\gamma^2R^*}, \tag{5}$$

$$\widetilde{R}_i = \frac{\partial R}{\partial x_i} = \gamma^2\left(\widetilde{R}_i^* - M_{\infty i}\right). \tag{6}$$

As the discrete sampling is given in practical measurements, the signal reception and emission time at discrete time steps t^k and τ^l are defined, respectively, as:

$$t^k = t^1 + (k-1)\Delta t, \quad k = 1,2,\ldots,K, \tag{7}$$

$$\tau^l = \tau^1 + (l-1)\Delta t, \quad l = 1,2,\ldots,L. \tag{8}$$

When the discrete pressure values are used to calculate the force values, the source time for each loading source should be determined via the retarded time relationship:

$$\tau_n^k = t^k - R_n/c. \tag{9}$$

Since the source time τ_n^k will not be in general an integer multiple of the given time interval Δt, the force component should be processed by the following time domain interpolation:

$$F_{ni}(\tau_n^k) = \sum_{l=1}^{k} \zeta^l(\tau_n^k) F_{ni}^l, \tag{10}$$

$$\dot{F}_{ni}(\tau_n^k) = \sum_{l=1}^{k} \frac{\partial \zeta^l(\tau_n^k)}{\partial \tau} F_{ni}^l, \tag{11}$$

where F_{ni}^l represents the force component at each source time step τ^l, and $\zeta^l(\tau_n^k)$ is the Lagrange linear interpolation function [44,45].

After the discretization and interpolation, Eq. (1) becomes:

$$p(\mathbf{x}, t^k) = \sum_{n=1}^{N} \sum_{l=1}^{k} g_{ni}^l(\tau_n^k) F_{ni}^l, \tag{12}$$

where $g_{ni}^l(\tau_n^k)$ is expressed as:

$$\begin{aligned} g_{ni}^l(\tau_n^k) = & \frac{\widetilde{R}_{ni}}{4\pi c_0 R_n^* (1 - M_{ni}\widetilde{R}_{ni})^2} \frac{\partial \zeta^l(\tau_n^k)}{\partial \tau} \\ & + \left[\frac{\widetilde{R}_{ni}^* - M_{ni}}{4\pi R_n^{*2} (1 - M_{ni}\widetilde{R}_{ni})^2} + \widetilde{R}_{ni} \frac{R_n^* \dot{M}_{ni} \widetilde{R}_{ni} + c_0 \left(M_{ni}\widetilde{R}_{ni}^* - M_n^2 \right)}{4\pi c_0 R_n^{*2} (1 - M_{ni}\widetilde{R}_{ni})^3} \right. \\ & - \widetilde{R}_{ni} \frac{M_{ni}\widetilde{R}_{ni}^* M_{ni}\widetilde{R}_{ni} + \gamma^2 \left((M_{\infty ni} M_{ni})^2 - \left(M_{ni}\widetilde{R}_{ni}^* \right)^2 \right)}{4\pi R_n^{*2} (1 - M_{ni}\widetilde{R}_{ni})^3}. \\ & \left. - \frac{\widetilde{R}_{ni}^* M_{ni}\widetilde{R}_{ni} + \gamma^2 \left(M_{\infty ni} M_{ni} M_{\infty ni} - \widetilde{R}_{ni}^* M_{ni}\widetilde{R}_{ni}^* \right)}{4\pi R_n^{*2} (1 - M_{ni}\widetilde{R}_{ni})^2} \right] \zeta^l(\tau_n^k) \end{aligned} \tag{13}$$

In a matrix form, Eq. (12) can be rewritten as:

$$p(\mathbf{x}, t^k) = \boldsymbol{\psi}^{1k}\mathbf{T}^1 + \boldsymbol{\psi}^{2k}\mathbf{T}^2 + \cdots + \boldsymbol{\psi}^{lk}\mathbf{T}^l + \cdots + \boldsymbol{\psi}^{kk}\mathbf{T}^k, \tag{14}$$

where

$$\begin{aligned} \boldsymbol{\psi}^{lk} = & \left[g_{11}^l(\tau_1^k) \quad \cdots \quad g_{N1}^l(\tau_N^k) \quad g_{12}^l(\tau_1^k) \quad \cdots, \right. \\ & \left. g_{N2}^l(\tau_N^k) \quad g_{13}^l(\tau_1^k) \quad \cdots \quad g_{N3}^l(\tau_N^k) \right] \end{aligned} \tag{15}$$

$$\mathbf{T}^l = \left[F_{11}^l \quad \cdots \quad F_{N1}^l \quad F_{12}^l \quad \cdots \quad F_{N2}^l \quad F_{13}^l \quad \cdots \quad F_{N3}^l \right]^{\mathrm{T}}. \tag{16}$$

By considering Q measurement points, and applying Eq. (14) to each measurement point, yields the following extended matrix equation:

$$\mathbf{P}^k = \mathbf{H}^{1k}\mathbf{T}^1 + \mathbf{H}^{2k}\mathbf{T}^2 + \cdots + \mathbf{H}^{lk}\mathbf{T}^l + \cdots + \mathbf{H}^{kk}\mathbf{T}^k, \tag{17}$$

where

$$\mathbf{P}^k = \left[p(\mathbf{x}_1, t^k) \quad p(\mathbf{x}_2, t^k) \quad \cdots \quad p(\mathbf{x}_q, t^k) \quad \cdots \quad p(\mathbf{x}_Q, t^k) \right]^{\mathrm{T}}, \tag{18}$$

$$\mathbf{H}^{lk} = \left[\left(\boldsymbol{\psi}_1^{lk} \right)^{\mathrm{T}} \quad \left(\boldsymbol{\psi}_2^{lk} \right)^{\mathrm{T}} \quad \cdots \quad \left(\boldsymbol{\psi}_q^{lk} \right)^{\mathrm{T}} \quad \cdots \quad \left(\boldsymbol{\psi}_Q^{lk} \right)^{\mathrm{T}} \right]^{\mathrm{T}}. \tag{19}$$

By applying Eq. (17) to each time step, yields a large matrix expression:

$$\mathbf{P} = \overleftrightarrow{\mathbf{H}} \overleftrightarrow{\mathbf{T}}, \tag{20}$$

where

$$\mathbf{P} = \left[\mathbf{P}^1 \quad \mathbf{P}^2 \quad \cdots \quad \mathbf{P}^k \quad \cdots \quad \mathbf{P}^K \right], \tag{21}$$

$$\overleftrightarrow{\mathbf{T}} = \left[\mathbf{T}^1 \quad \mathbf{T}^2 \quad \cdots \quad \mathbf{T}^k \quad \cdots \quad \mathbf{T}^K \right], \tag{22}$$

$$\overleftrightarrow{\mathbf{H}} = \begin{bmatrix} \mathbf{H}^{11} & & & & & \\ \mathbf{H}^{12} & \mathbf{H}^{22} & & & & \\ \vdots & \vdots & \ddots & & & \\ \mathbf{H}^{1k} & \mathbf{H}^{2k} & \cdots & \mathbf{H}^{kk} & & \\ \vdots & \vdots & \ddots & \vdots & \ddots & \\ \mathbf{H}^{1K} & \mathbf{H}^{2K} & \cdots & \mathbf{H}^{kK} & \cdots & \mathbf{H}^{KK} \end{bmatrix}. \tag{23}$$

Eq. (20) is a linear system that relates the force components in the three directions of the N discrete forces along the blades in moving medium and at different source time steps to Q microphone acoustic pressures at different observer time steps. Then, the force components at different locations on the rotor disk and at different source time steps can be computed from the sampled values of the acoustic pressure at the measurement points by inverting Eq. (20) as:

$$\overleftrightarrow{\mathbf{T}} = \overleftrightarrow{\mathbf{H}}^{+}\mathbf{P}, \tag{24}$$

where the superscript "+" denotes the pseudo-inverse of a matrix $\overleftrightarrow{\mathbf{H}}$. This inverse problem is usually ill-conditioned when numerical parameters are chosen inappropriately [46,47], such as the number and positions of source points, the time step, and the distance between the source surface and the measurement surface, etc. An in-depth investigation about the factors affecting the condition number of the transfer matrix has been done by Nelson and Yoon in the Refs. [46,47]. Among these factors, the distance between the equivalent source surface and the measurement surface plays a very important role in affecting the condition number. The smaller the distance is, the smaller the condition number is. Thus, in order to keep lower condition number and obtain higher reconstruction accuracy, it is better to measure the acoustic pressure in the near field.

In order to suppress the ill-posed problem in the inversion process, regularization should be done to guarantee accurate solutions [48,49]. Considering that the reconstructed unsteady rotating forces have different characteristics in space and time: force application points are concentrated in space, while force signals vary continuously in time, and there are $3N$ unknowns to be solved at every source time step, which is usually more than the number of microphones Q in practical measurements, a space-time regularization with a mixed $l_{1,2}$-norm term is used in this paper. The method takes advantage of the spatial sparsity of the excitation field and the continuity of the time signals by combining an l_1-norm in space and an l_2-norm in time, thus allowing to reconstruct the forces accurately when the number of input signals is less than the number of unknowns.

2.2. Space-time regularization with a mixed $l_{1,2}$-norm term

The space-time regularization with a mixed $l_{1,2}$-norm term is introduced in the inverse problem framework [50,51], namely

$$\widetilde{\mathbf{T}} = \underset{\overleftrightarrow{\mathbf{T}}}{\operatorname{argmin}} \| \overleftrightarrow{\mathbf{P}} - \overleftrightarrow{\mathbf{H}}\,\overleftrightarrow{\mathbf{T}} \|_2^2 + \lambda \| \widehat{\mathbf{T}} \|_{1,2}^2, \tag{25}$$

$$\widehat{\mathbf{T}} = \begin{bmatrix} (\mathbf{T}^1)^{\mathrm{T}} \\ (\mathbf{T}^2)^{\mathrm{T}} \\ \vdots \\ (\mathbf{T}^k)^{\mathrm{T}} \\ \vdots \\ (\mathbf{T}^K)^{\mathrm{T}} \end{bmatrix}^{\mathrm{T}} = \begin{bmatrix} F_{11}^1 & F_{11}^2 & \cdots & F_{11}^k & \cdots & F_{11}^K \\ \vdots & \vdots & \ddots & \vdots & \ddots & \vdots \\ F_{N1}^1 & F_{N1}^2 & \cdots & F_{N1}^k & \cdots & F_{N1}^K \\ F_{12}^1 & F_{12}^2 & \cdots & F_{12}^k & \cdots & F_{12}^K \\ \vdots & \vdots & \ddots & \vdots & \ddots & \vdots \\ F_{N2}^1 & F_{N2}^2 & \cdots & F_{N2}^k & \cdots & F_{N2}^K \\ F_{13}^1 & F_{13}^2 & \cdots & F_{13}^k & \cdots & F_{13}^K \\ \vdots & \vdots & \ddots & \vdots & \ddots & \vdots \\ F_{N3}^1 & F_{N3}^2 & \cdots & F_{N3}^k & \cdots & F_{N3}^K \end{bmatrix}. \tag{26}$$

Where $\widehat{\mathbf{T}}$ is the matrix rewritten by the elements of the unknown force vector $\overleftrightarrow{\mathbf{T}}$ in Eq. (22). The rows correspond to the time signal at a particular location and the columns to the excitation field at a specific instant. The minimization problem in Eq. (25) can be solved by the generalized iterative reweighted least squares algorithm [52] by transforming $\| \widehat{\mathbf{T}} \|_{1,2}^2$ to $\| \widehat{\mathbf{W}}\,\overleftrightarrow{\mathbf{T}} \|_2^2$, where $\widehat{\mathbf{W}}$ is a diagonal matrix and its element is $\sqrt{W_{ni}^k W^k}$.

$$W_{ni}^k = \begin{cases} \left|F_{ni}^k\right|^{1-2} & , \left|F_{ni}^k\right| \geq \varepsilon \\ \varepsilon^{1-2} & , \text{otherwise} \end{cases} \tag{27}$$

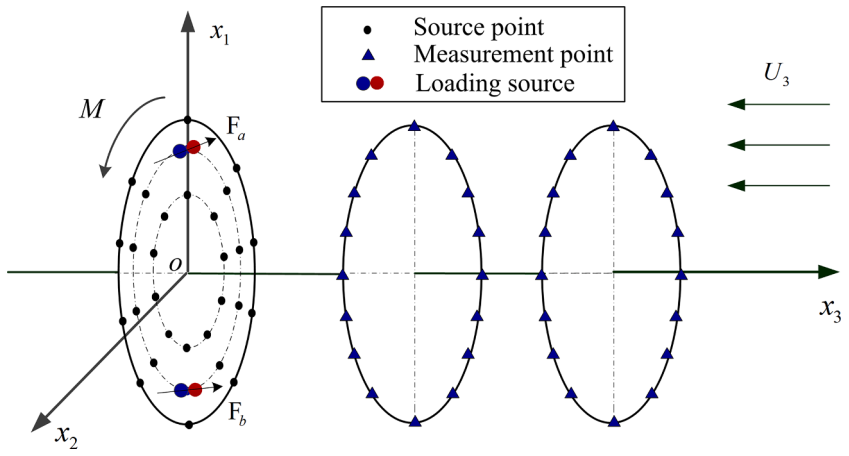

Fig. 2. Geometric description of the rotating loading sources, source points, measurement points and prediction points. U_3 is the axial flow velocity in the x_3 direction.

$$W^k = \begin{cases} \left[\| \left(\mathbf{T}^k\right)^{\mathrm{T}} \|_1^1 \right]^{2/1-1} & , \| \left(\mathbf{T}^k\right)^{\mathrm{T}} \|_1^1 \geq \varepsilon^2 \\ \left(\varepsilon^2\right)^{2/1-1} & , \text{otherwise} \end{cases} \tag{28}$$

To avoid infinite weights, a small real positive number ε is added to W_{ni}^k and W^k, respectively. The explicit solution of Eq. (25) can be expressed in the following form:

$$\widetilde{\mathbf{T}} = \left(\overleftrightarrow{\mathbf{H}}^{\mathrm{H}} \overleftrightarrow{\mathbf{H}} + \lambda \overleftrightarrow{\mathbf{W}} \right)^{-1} \overleftrightarrow{\mathbf{H}}^{\mathrm{H}} \overleftrightarrow{\mathbf{P}}, \tag{29}$$

where $\overleftrightarrow{\mathbf{W}} = \widehat{\mathbf{W}}^{\mathrm{H}} \widehat{\mathbf{W}}$, the symbol "H" means the Hermitian transpose. Since the weighting matrix $\overleftrightarrow{\mathbf{W}}$ requires an iterative process while obtaining the solution of the minimization problem. The solution $\widetilde{\mathbf{T}}^{(s)}$ at iteration s relies on solution at iteration $s-1$, namely

$$\widetilde{\mathbf{T}}^{(s)} = \left(\overleftrightarrow{\mathbf{H}}^{\mathrm{H}} \overleftrightarrow{\mathbf{H}} + \lambda \overleftrightarrow{\mathbf{W}}^{(s-1)} \right)^{-1} \overleftrightarrow{\mathbf{H}}^{\mathrm{H}} \overleftrightarrow{\mathbf{P}}, \tag{30}$$

where $\overleftrightarrow{\mathbf{W}}^{(s-1)}$ is composed of the exciting force F_{ni}^k at iteration $s-1$. The initial solution $\widetilde{\mathbf{T}}^{(0)}$ of the iterative procedure is estimated based on the standard Tikhonov regularization [48], i.e.,

$$\widetilde{\mathbf{T}}^{(0)} = \underset{\overleftrightarrow{\mathbf{T}}}{\operatorname{argmin}} \| \overleftrightarrow{\mathbf{P}} - \overleftrightarrow{\mathbf{H}} \overleftrightarrow{\mathbf{T}} \|_2^2 + \lambda \| \overleftrightarrow{\mathbf{T}} \|_2^2. \tag{31}$$

Where λ is determined according to the L-curve criterion [53]. The functional Γ at iteration s is given by

$$\Gamma\left(\widetilde{\mathbf{T}}^{(s)}\right) = \| \overleftrightarrow{\mathbf{P}} - \overleftrightarrow{\mathbf{H}} \widetilde{\mathbf{T}}^{(s)} \|_2^2 + \lambda \| \overleftrightarrow{\mathbf{W}}^{(s-1)} \widetilde{\mathbf{T}}^{(s)} \|_2^2. \tag{32}$$

As a result, the relative variation δ of the functional Γ between two adjacent iterations can be expressed as:

$$\delta = \left| 1 - \frac{\Gamma\left(\widetilde{\mathbf{T}}^{(s)}\right)}{\Gamma\left(\widetilde{\mathbf{T}}^{(s-1)}\right)} \right|. \tag{33}$$

The algorithm is re-iterated until the relative variation is less than or equal to a given tolerance or the maximum number of iterations is reached.

For the sake of clarity, it is worth mentioning that the present method treats constant rotating forces, which are unsteady in the microphone absolute reference system, and forces that are unsteady in the rotating reference system in the same way. Therefore, the method is able to compute equivalent unsteady rotating forces in a generic sense, with both rotational Doppler effects and mean-flow acoustic convective effects taken into account by the underlying acoustic analogy model.

3. Numerical verification study

Numerical simulations have been initially carried out to examine the performance of the proposed method for reconstructing the unsteady rotating forces in moving medium and the results of the performed verification tests are reported and discussed in this

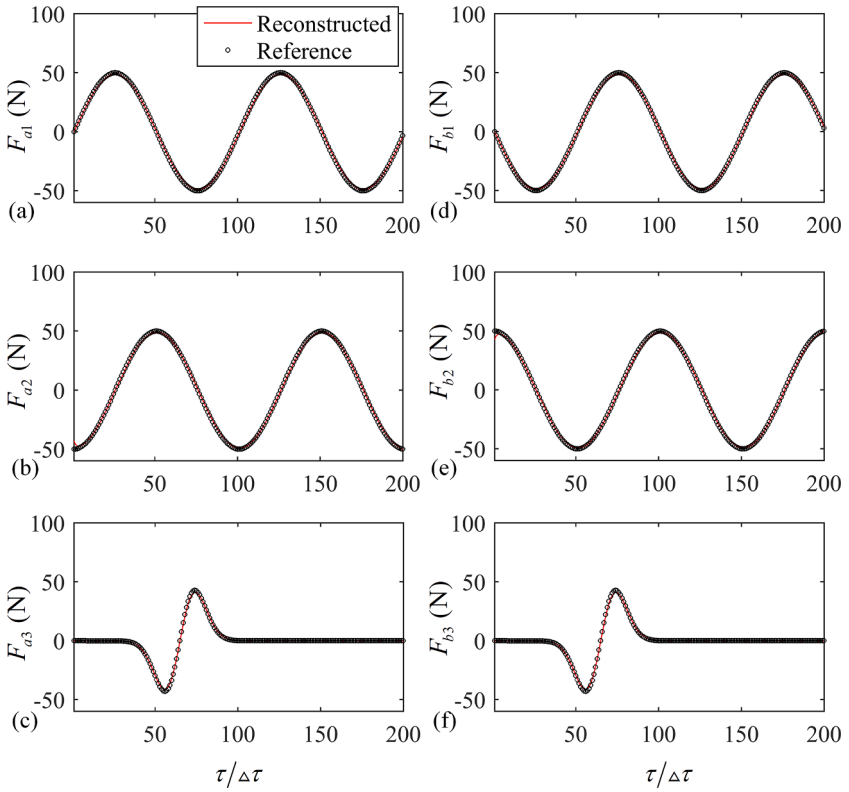

Fig. 3. Comparison of the reconstructed and reference unsteady force components of F_a (left) and F_b (right) for an axial flow velocity of 40 m/s.

section.

The layout of the rotor model is sketched in Fig. 2, where a number of 30 source points are equally distributed along three rings with a radius of 0.1, 0.2 and 0.3 m. These source points have identical rotational speed Ω=1020 RPM. In order to improve the accuracy of the force reconstruction for a given number of source points, it is important to locate source points at radial distances corresponding to locations of actual high blade loading. Therefore, the present numerical verification test is performed by using the pressure signals generated by two forces F_a and F_b initially located at the points (0.2, 0, 0) m and (-0.2, 0, 0) m, respectively, as an input. The Cartesian coordinates $o(x_1, x_2, x_3)$ is depicted in Fig. 2. These two positions coincide with two equivalent source positions on the second ring.

In order to quantify the reconstruction error of the proposed method, the phase evaluation indicator E_p and the amplitude evaluation indicator E_a are used, which are defined, respectively, by [54]

$$E_p = \frac{\left|\mathbf{F}_{\mathrm{th}}^{\mathrm{T}}\mathbf{F}_{re}\right|}{\sqrt{\left(\mathbf{F}_{\mathrm{th}}^{\mathrm{T}}\mathbf{F}_{th}\right)\left(\mathbf{F}_{\mathrm{re}}^{\mathrm{T}}\mathbf{F}_{re}\right)}}, \tag{34}$$

$$E_a = \frac{\left|\sqrt{\mathbf{F}_{\mathrm{th}}^{\mathrm{T}}\mathbf{F}_{th}} - \sqrt{\mathbf{F}_{\mathrm{re}}^{\mathrm{T}}\mathbf{F}_{re}}\right|}{\sqrt{\mathbf{F}_{\mathrm{re}}^{\mathrm{T}}\mathbf{F}_{re}}}, \tag{35}$$

where the superscript "T" denotes the transpose of matrix; $\mathbf{F}_{\mathrm{th}}$and $\mathbf{F}_{\mathrm{re}}$ are the theoretical and reconstructed forces, respectively. A phase indicator E_p approaching the unitary value indicates a high phase similarity between the effective and reconstructed force signals, whereas an amplitude indicator E_a approaching zero indicates a vanishing amplitude error.

The three components of the two unsteady rotating forces F_a^{th} and F_b^{th} in the Cartesian coordinate system $o(x_1, x_2, x_3)$ are expressed as [38]:

$$F_a^{th}\begin{cases} F_{a1}^{th} = F_D\sin(\phi_1 + \Omega\tau) \\ F_{a2}^{th} = -F_D\cos(\phi_1 + \Omega\tau) \\ F_{a3}^{th} = F_L = C((\tau-\tau_o)/T_v)\exp\left(-(\tau-\tau_o)^2/T_v^2\right) \end{cases}, \tag{36}$$

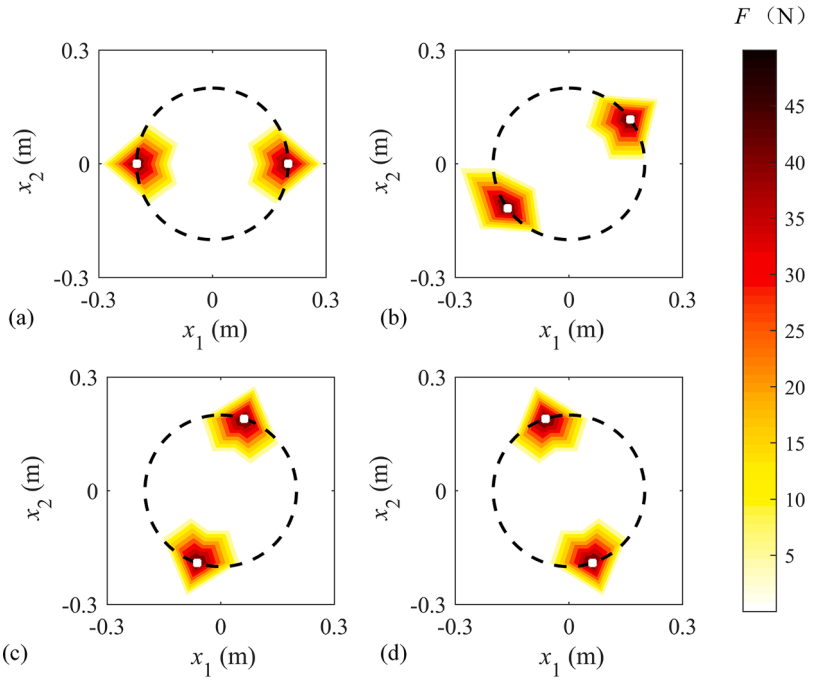

Fig. 4. Spatial distribution of the reconstructed forces at four selected time steps: (a) τ_1; (b) τ_{11}; (c) τ_{21}; (d) τ_{31}. The white squares indicate the real positions of two loading sources.

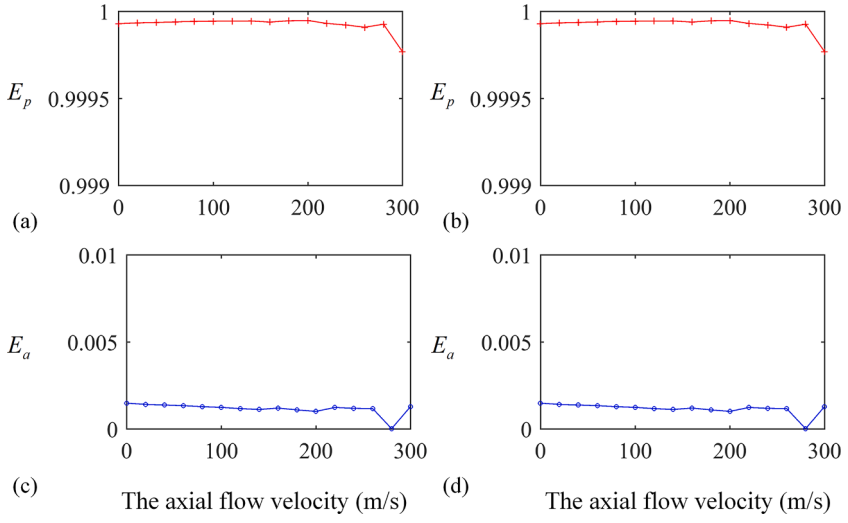

Fig. 5. The phase indicator E_p and the amplitude indicator E_a of the unsteady rotating forces F_a (left); and F_b (right).

$$F_b^{th}\begin{cases} F_{b1}^{th} = F_D\sin(\phi_2 + \Omega\tau) \\ F_{b2}^{th} = -F_D\cos(\phi_2 + \Omega\tau) \\ F_{b3}^{th} = F_L = C((\tau-\tau_o)/T_v)\exp\left(-(\tau-\tau_o)^2/T_v^2\right) \end{cases}, \tag{37}$$

where ϕ_1 and ϕ_2 are the initial phases of two unsteady rotating loading sources, respectively; F_D is the magnitude of the drag force; F_L is the magnitude of the thrust force; C is a constant number; τ_o is the pulse time delay and T_v is the pulse time spreading width. The specific parameter values are given as $F_D = 50$ N, $C = 100$, $\phi_1 = 0$, $\phi_2 = \pi$, $\Omega = 2\pi\widehat{N}/60$, $\widehat{N} = 1020$RPM, $\tau_o = 64\Delta t$, and $T_v = 12.8\Delta t$, with the time step $\Delta t = 1/1700$ s, corresponding to 100 time steps per revolution.

The acoustic pressure measurement array consists in 60 microphones equally distributed on two rings of the same radius of 0.25 m located on planes parallel to the rotor disk, as shown in Fig. 2. The two rings are located at an axial distance of 0.02 m and 0.04 m from

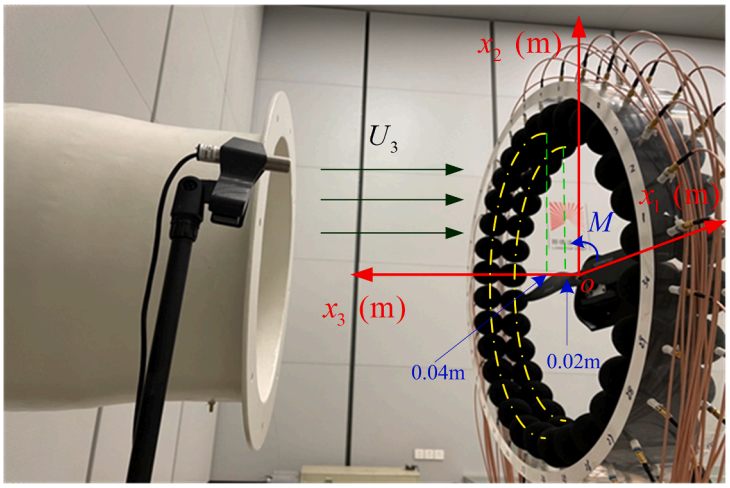

Fig. 6. Experimental setups for measuring the UAV rotating blade noise in uniform flow: the wind tunnel, the UAV blades, the microphone array, and the laser speedometer.

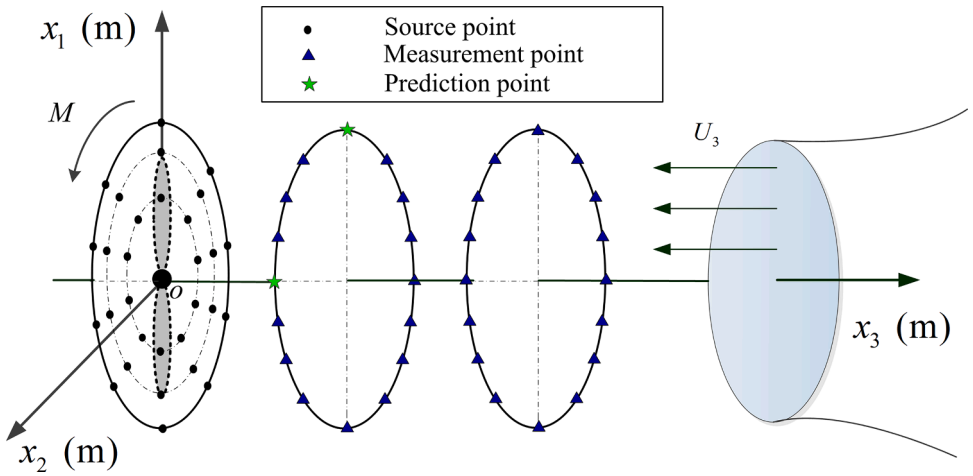

Fig. 7. Geometric description of the rotating blades, wind tunnel, source points, measurement points and prediction points. Axial coordinate not in scale. The distances between the two ring subarrays from the propeller plane are 0.02 m and 0.04 m, respectively.

the rotor disk, respectively. The axial flow velocity is set to the value of 40 m/s, corresponding to a Mach number of 0.12 for an ambient sound speed of 340 m/s. Based on the above simulation settings, the radiated sound pressure of the rotating loading sources, as input, can be calculated from Eq. (1). Additional Gaussian white noise with a signal-to-noise ratio of 30 dB is added to the pressure signals for simulating realistic conditions and better stressing the robustness of the method. Since the real values of the two unsteady rotating forces are known in the simulations, they are used as reference for comparison.

Fig. 3 shows the comparison between the reconstructed and reference force time histories. A very good qualitative agreement can be observed during the entire time period. For a quantitative evaluation of the reconstruction accuracy, the calculated values of the phase and amplitude indices are 0.0014 and 0.9999, respectively, with identical values for the two forces.

In order to better visualize the spatial localization results of the proposed methods, the source maps at the time steps of τ_1, τ_{11}, τ_{21} and τ_{31} are shown in Fig. 4. The white squares indicate the real instantaneous positions of the two loading sources. It can be observed that the proposed method can accurately localize the unsteady loading sources at different time steps.

Having stated the accuracy of the inverse method at a given axial flow velocity, the convergence characteristics of the proposed method are further investigated by evaluating the accuracy indicators at different values of the axial flow velocity, from 0 to 300 m/s, corresponding to a maximum convective Mach number of 0.88. Due to the numerical nature of the present verification test, the range of inflow Mach number can be extended beyond typical operational conditions. Fig. 5 shows the phase and amplitude indicators obtained at different axial flow velocities. It can be observed that the phase indicators are close to 1 and the amplitude indicators are close to 0, which indicates that the proposed method achieves a very accurate and robust reconstruction at all values of the axial flow velocity. Even when the axial flow velocity reaches very high values, the proposed method can still yield a satisfactory reconstruction

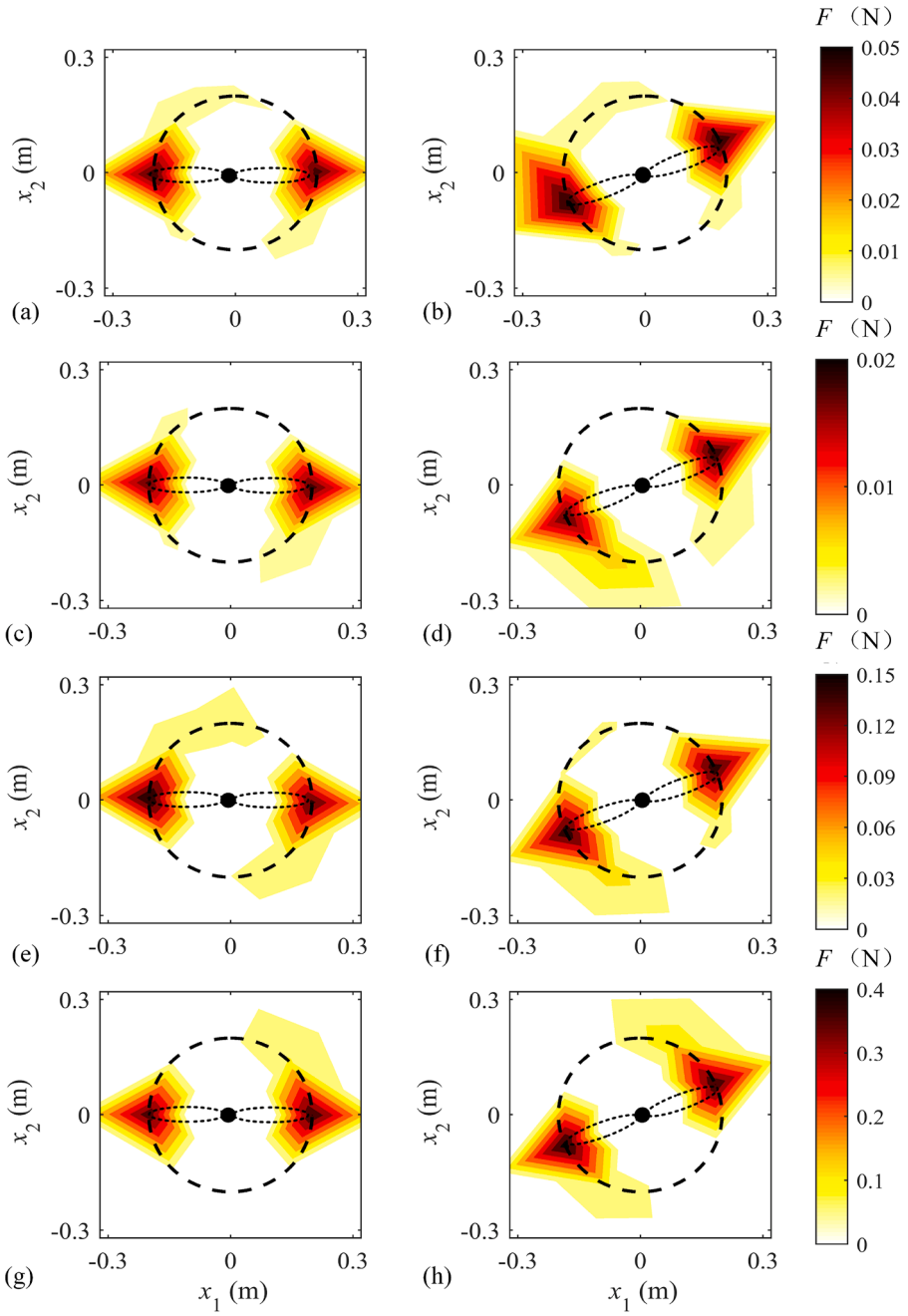

Fig. 8. The localization results of the two rotating blades at time step τ_{615} for the axial flow velocities of 0 m/s (a), 5 m/s (c), 10 m/s (e), 20 m/s (g); and at time step τ_{683} for the axial flow velocities of 0 m/s (b), 5 m/s (d), 10 m/s (f), 20 m/s (h).

accuracy.

4. Experimental validation study

To validate the proposed inverse method for rotating forces exerted by the rotor blades in a moving medium, experiments with UAV rotor have been carried out in an open wind tunnel and the results are reported and discussed in this section.

The test rig installed in the semi-anechoic aeroacoustic wind tunnel in Hefei University of Technology is shown in Fig. 6. The flow comes from the circular nozzle installed on the test chamber. The nozzle diameter is 0.4 m. The height of the test chamber is 8.5 m, and the other two dimensions are 7.6 and 5.5 m. The cut-off frequency of the chamber is approximately 63 Hz. The turbulence level in the core of jet is below 0.5% and flow non-uniformity in the nozzle area is below 0.1% for the nozzle exit velocity of 20 m/s. The blades are

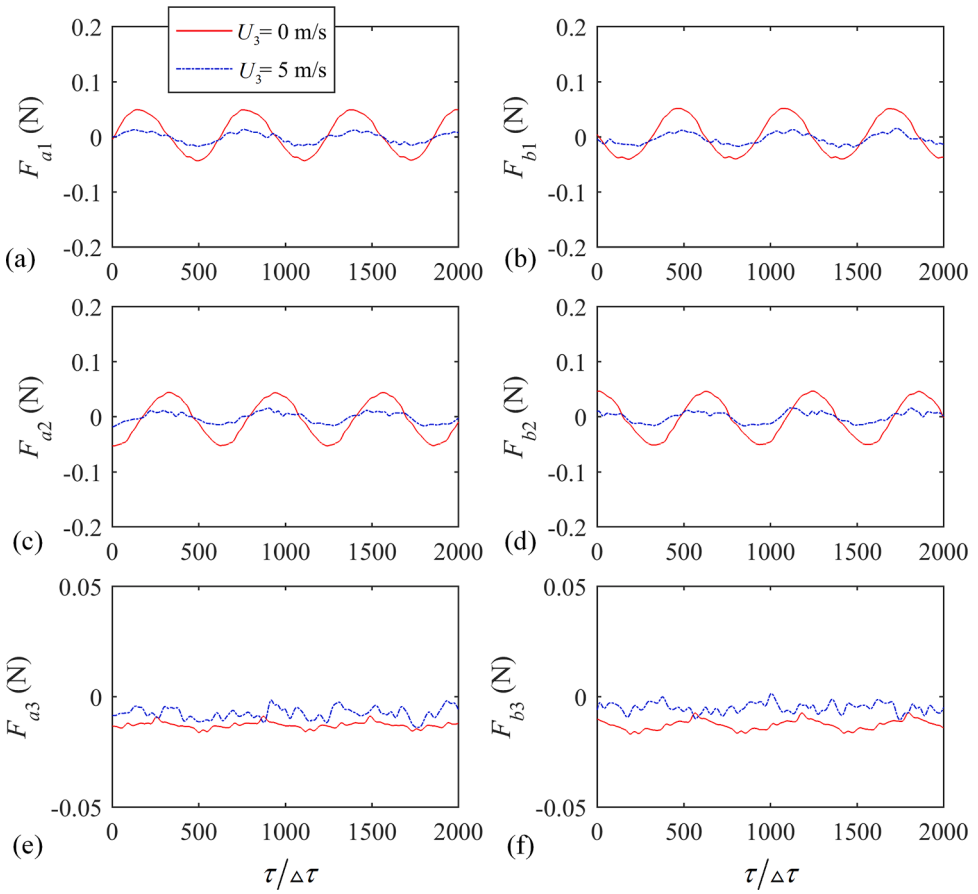

Fig. 9. The reconstructed force components in the three directions on the tip of two rotating blades (source ring radius of 0.2 m) for the axial flow velocities of 0 and 5 m/s.

connected to a cylindrical brushless motor with a diameter of 6 cm for minimum interference with the propeller flow. The support structure of blades is fixed outside the wind tunnel outlet. The entire support structure is very stiff and submitted to almost no vibration when the rotor is operated in axial flow conditions, as in the present preliminary campaign.

As shown in Fig. 7, the blade planform is discretized into a series of source points. These source points are distributed along three rings with the radius of 0.1, 0.2 and 0.3 m. Each ring contains 10 source points. The unsteady loading sources at these points are supposed to rotate at the same rotational speed as the blades. The propeller diameter D is 0.4 m, the same value as the nozzle diameter.

A laser speedometer is used to measure the blade tip speed, which is 997.25 RPM, corresponding to a tip Mach number of 0.062. The distance between the rotor plane and the jet nozzle plane is about 0.5 m. Therefore, part of the rotor blade is located in the shear layer of the jet. By assuming a laminar core length of 5 nozzle diameters, a blade tip segment of about 0.05 m, i.e., a quarter radius, is located in a highly sheared, and potentially unstable, flow region. This is therefore a potential source of loading unsteadiness, and certainly a more severe validation condition compared to the verification study carried out in the previous section. The propeller is operated by varying the free-stream axial flow velocity in the jet wind tunnel. In the present study, the results for the jet exit velocities U_3 of 0 m/s, 5 m/s, 10 m/s and 20 m/s are considered, respectively. These correspond to values of the advance ratio $J = 60U_3/(\widehat{N}\mathrm{D})$ of 0, 0.75, 1.5 and 3, respectively.

The microphone array is the same as the one employed in the numerical simulation tests. The double-ring array consists of 60 high-precision microphones (BSWA MPA 451) with the sensitivity of -50 $\pm$ 5 dBV/Pa. The diameter of the array is 0.5 m. The distances between the two ring subarrays from the propeller plane are 0.02 m and 0.04 m, respectively. A Müller-BBM acquisition instrument with 60-bit cards is used to simultaneously sample the 60-channels of microphones at 10.24 k samples/s. In order to avoid contamination of the noise measurements to the pseudo-sound generation by the flow interacting with the microphones, these have been located outside the laminar core of the jet, but sufficiently close to the jet axis to assume acoustic propagation in a constant mean flow in the underlying acoustic analogy model. At present stage of the research, the impact of this modeling assumption, as well as the effects related to the steady and unsteady refraction due to the jet shear-layer, have not been evaluated. Since the microphones are relatively close to the jet shear layer, wind proof balls have been added to the microphones, and this ensures a higher signal-to-noise ratio of the unsteady loading noise contribution, which are expected to be generated by stochastic variations of the inflow angle of attack induced by impinging vortical structures [38].

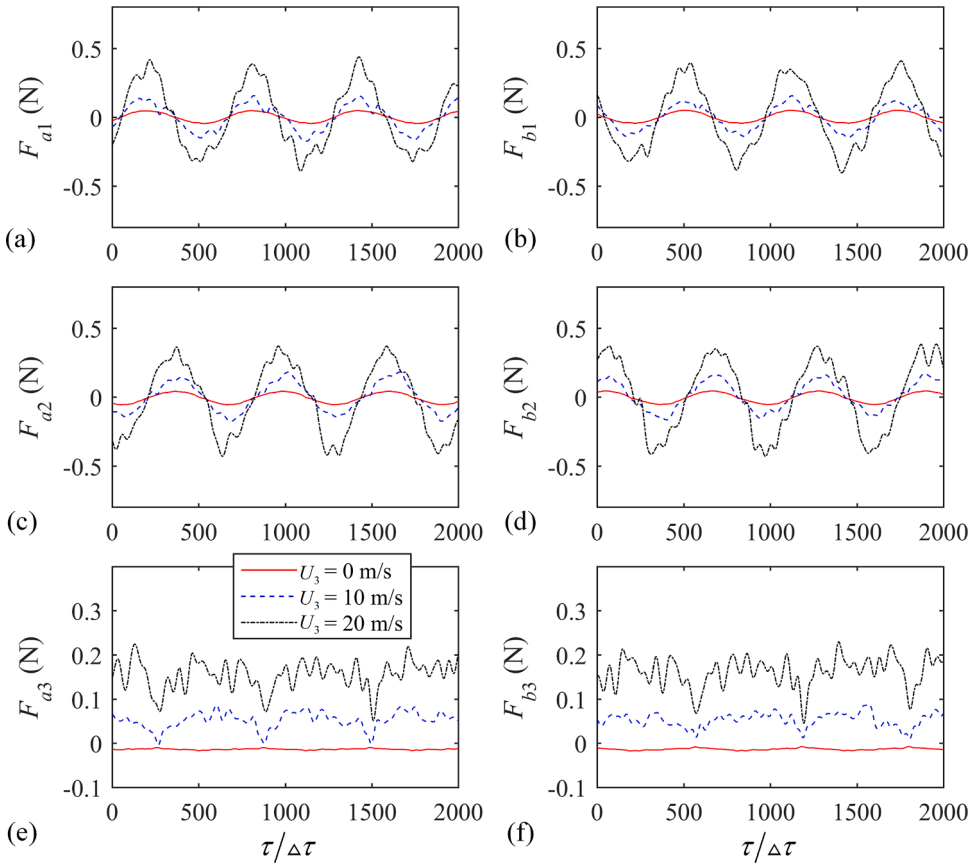

Fig. 10. The reconstructed force components in the three directions on the tip of two rotating blades (source ring radius of 0.2 m) for the axial flow velocities of 0, 10 and 20 m/s.

Fig. 8 shows the localization results of unsteady loading sources on the rotating blades at two different time steps τ_{615} and τ_{683}, obtained for the four values of axial flow velocity. It can be seen that the proposed method can clearly locate the unsteady loading sources on the rotating blades at two selected time steps in the uniform flow, and the loading sources mainly concentrate at the tips of the blades, where the change rate of the Mach number projected along the observer direction and the surface velocity are high, and where the aerodynamic force magnitudes are high. As expected, the loading sources in the blade tip region are the most significant contributor to the radiated noise field.

Figs. 9 and 10 show the time histories of unsteady rotating forces on the blade tips, obtained for the four values of axial flow velocity. It can be observed that when the flow velocity is 0 m/s, the reconstructed force components in both x_1 and x_2 directions exhibit the sine and cosine harmonic form due to the projection of the drag force component at different azimuthal locations of the blade. The difference between the initial phases of the unsteady forces on two rotating blades is 180°. As shown in Fig. 9, at the axial flow velocity of 5 m/s ($J = 0.75$), the amplitude of the reconstructed drag-force components is lower than that for the 0 m/s case ($J = 0$). As expected, both torque and thrust components decrease with increasing rotor advance ratios due to a reduction of the sectional flow incidence. The same trend can be observed for the axial force component, which exhibits a slightly lower amplitude for the non-zero advance ratio case. Moreover, the non-zero flow case reveals high level of unsteadiness, which is likely due to the interaction between the rotor tip and the jet shear layer. It can be finally observed, that for both advance ratios a negative mean axial force component is predicted, which indeed indicate a positive thrust generated by the rotor.

At higher values of the advance ratio, the reconstructed force time histories plotted in Fig. 10 exhibit a different trend: the amplitudes of all force components increase with an increasing advance ratio and a negative thrust is generated. Indeed, for jet flow velocities higher than 5 m/s, the rotor operates in windmill conditions and the negative sectional flow incidence is prone of flow separation. The high level of force fluctuations can be therefore due to a combination of flow separation and blade tip interaction with a highly unsteady jet shear layer. The relative contribution of these two effects will be evaluated in future steps of the present research.

The reconstruction accuracy of the unsteady rotating forces acting by rotor blades in moving medium is further evaluated by comparing the predicted sound signals with the measured ones. Fig. 11 shows the comparison of the sound pressures at two prediction points M1 (0.2, 0, 0.02) m and M2 (0, 0.2, 0.02) m, for the four values of the axial flow velocity. It can be argued that the predicted results are in good agreement with the measured ones, except for the occurrence of additional low-amplitude fluctuations in the reconstructed signals. As shown in Fig. 11(a)–(d), where noise signals for the 0 and 5 m/s cases are plotted, the dynamics of the signals

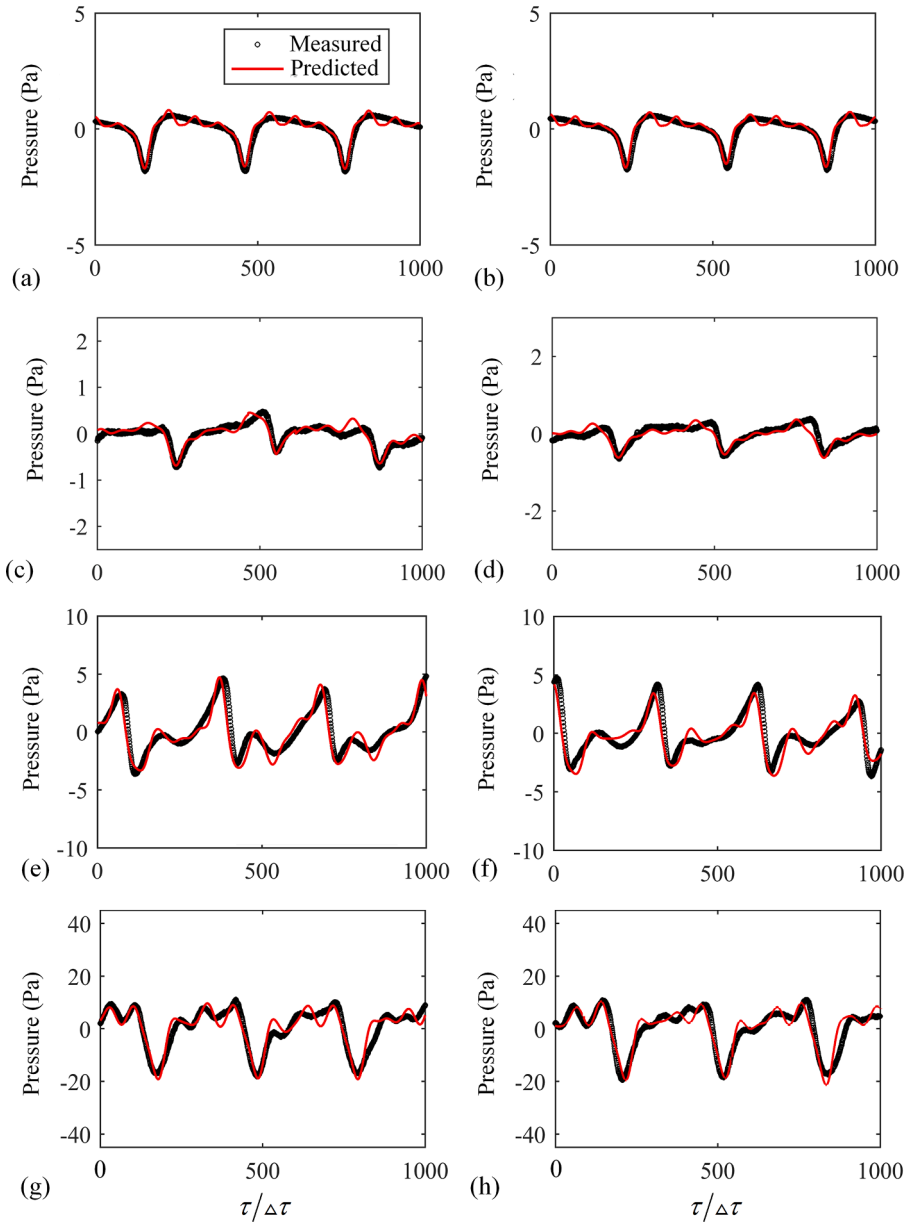

Fig. 11. Comparison of the predicted and measured pressures at prediction point M1 (0.2, 0, 0.02) m for the axial flow velocities of 0 m/s (a), 5 m/s (c) 10 m/s (e), 20 m/s (g); and at prediction point M2 (0, 0.2, 0.02) m for the axial flow velocities of 0 m/s (b), 5 m/s (d), 10 m/s (f), 20 m/s (h).

Table 1
Phase and amplitude accuracy indicators at different jet flow velocities.

U_3	0 m/s	5 m/s	10 m/s	20 m/s
E_p	0.9157	0.9122	0.9086	0.9126
E_a	0.0128	0.0542	0.0652	0.0859

are lower for the non-zero advance ratio case, in agreement with the predicted lower force fluctuations. Conversely, the dynamics of the noise signals significantly increase with the advance ratio at velocities higher than 5 m/s, as shown in Fig. 11(e)–(h).

In order to evaluate the accuracy of the force reconstruction for the present validation case, the phase and amplitude indicators are computed and reported in Table 1. It can be argued that the phase error is weakly influenced by the free-stream velocity, whereas the amplitude error increases with the jet velocity. These results confirm that the proposed inverse method can achieve accurate and robust reconstruction of the sound fields also in conditions of intense force fluctuations, as in the case of a rotor operating in windmill

conditions and partially located in the shear layer of a jet flow.

5. Conclusions

This paper presented a time-domain inverse aeroacoustic method based on the convective FW-H equation to reconstruct unsteady rotating forces exerted by rotor blades in moving medium. In this method, the analytical direct model that relates the unsteady rotating forces to the radiated sound field is first discretized, and then the unsteady rotating forces are reconstructed from the measured pressures via a time-domain inversion procedure, where space-time regularization with a mixed $l_{1,2}$-norm is employed to properly tackle both spatial localization and temporal reconstruction problems simultaneously. The influence of the convected moving medium on rotating aeroacoustic sources is studied and further clarified based on the proposed method. In a first step, numerical simulations of unsteady rotating point forces in moving medium were performed to verify the effectiveness of the proposed method. In addition, the convergence characteristics of the proposed method were investigated through simulations by estimating the accuracy indicators at increasing values of the axial flow velocity, from 0 to 300 m/s. In a second step, experiments with UAV rotor blades were carried out in an open wind tunnel for the jet exit velocities of 0, 5, 10 and 20 m/s. The results indicated that at lower rotor advance ratios, both torque and thrust components decrease at increasing values of the advance ratio, due to a reduction of the sectional flow incidence. Conversely, at high values of the advance ratio, the amplitude of the drag component increases at increasing values of the advance ratio. This effect is likely due the onset of flow separation. Moreover, the inflow turbulence developing in the shear layer of the jet, whose intensity increases with the jet velocity, is an additional possible source of unsteady loading. The accuracy of the reconstructed noise signals based on the sources computed by the inverse method is similar for the four values of the free-stream velocity.

The next steps of the current research will focus on the characterization of the shear-layer contamination effects and the associated uncertainties in the force reconstruction, and to a validation of the predicted unsteady loading through a high-fidelity numerical simulation of the experimental rig.

CRediT authorship contribution statement

Ying Xu: Methodology, Validation, Formal analysis, Investigation. **Damiano Casalino:** Conceptualization, Methodology, Writing – review & editing. **Xiao-Zheng Zhang:** Conceptualization, Methodology, Software, Writing – original draft. **Yong-Bin Zhang:** Supervision, Software, Writing – original draft. **Chuan-Xing Bi:** Supervision, Conceptualization, Methodology, Writing – review & editing.

Declaration of Competing Interest

The authors declare that they have no known competing financial interests or personal relationships that could have appeared to influence the work reported in this paper.

Data availability

Data will be made available on request.

Acknowledgments

This work was supported by the National Natural Science Foundation of China (Grant No. 12174082).

The authors thank Liang-He Li, Cheng-Hao Yang and other researchers who helped complete the experimental platform construction of this manuscript.

The authors thank the two anonymous reviewers and preliminary editor whose comments helped improve the clarity of this manuscript.

References

[1] D. Casalino, W. Velden, G. Romani, Community noise of urban air transportation vehicles, in: Proceedings of the AIAA Aerospace Sciences Meeting, 2019, https://doi.org/10.2514/6.2019-1834, 2019–1834.

[2] D. Casalino, W. Velden, G. Romani, I. Gonzalez-Martino, Aeroacoustic analysis of urban air operations using the LB/VLES method, in: Proceedings of the 25th AIAA/CEAS Aeroacoustics Conference, 2019, https://doi.org/10.2514/6.2019-2662, 2019–2662.

[3] Y. Fuerkaiti, D. Casalino, F. Avallone, D. Ragni, Aircraft community noise prediction in 3D environments using Gaussian beam tracing, in: Proceedings of the 28th AIAA/CEAS Aeroacoustics 2022 Conference, 2022, https://doi.org/10.2514/6.2022-3079, 2022–3079.

[4] J.E. Ffowcs Williams, D.L. Hawkings, Sound generated by turbulence and surfaces in arbitrary motion, Philos. Trans. R. Soc. A 264 (1969) 321–342, https://doi.org/10.1098/rsta.1969.0031.

[5] F. Farassat, G.P. Succi, The prediction of helicopter discrete frequency noise, Vertica 7 (4) (1983) 309–320, https://doi.org/10.2514/3.45598.

[6] K.S. Brentner, An efficient and robust method for predicting helicopter high-speed impulsive noise, J. Sound Vib. 203 (1) (1997) 87–100, https://doi.org/10.1006/jsvi.1996.0834.

[7] P.D. Francescantonio, A new boundary integral formulation for the prediction of sound radiation, J. Sound Vib. 202 (1997) 491–509, https://doi.org/10.1006/jsvi.1996.0843.

[8] D. Casalino, An advanced time approach for acoustic analogy predictions, J. Sound Vib. 261 (2003) 583–612, https://doi.org/10.1016/S0022-460X(02)00986-0.
[9] G. Ghorbaniasl, C. Lacor, A moving medium formulation for prediction of propeller noise at incidence, J. Sound Vib. 331 (2012) 117–137, https://doi.org/10.1016/j.jsv.2011.08.018.
[10] D. Casalino, E. Grande, G. Romani, D. Ragni, F. Avallone, Definition of a benchmark for low reynolds number propeller aeroacoustics, Aerosp. Sci. Technol. 113 (2021), 106707, https://doi.org/10.1016/j.ast.2021.106707.
[11] C.S.T. Envelope, Computational study of boundary layer effects on stochastic rotor blade vortex shedding noise, Aerosp. Sci. Technol. 131 (2022), 107983, https://doi.org/10.1016/j.ast.2022.107983.
[12] D. Casalino, G. Romani, R. Zhang, H. Chen, Lattice-boltzmann calculations of rotor aeroacoustics in transitional boundary layer regime, Aerosp. Sci. Technol. 130 (2022), 107953, https://doi.org/10.1016/j.ast.2022.107953.
[13] G. Romani, E. Grande, F. Avallone, D. Ragni, D. Casalino, Computational study of flow incidence effects on the aeroacoustics of low blade-tip mach number propellers, Aerosp. Sci. Technol 120 (2022), 107275, https://doi.org/10.1016/j.ast.2021.107275.
[14] C. Nardari, D. Casalino, F. Polidoro, V. Coralic, J. Brodie, P.T. Lew, Numerical and experimental investigation of flow confinement effects on UAV rotor noise, in: Proceedings of the 25th AIAA/CEAS Aeroacoustics Conference, 2019, https://doi.org/10.2514/6.2019-2497, 2019–2497.
[15] D. Kim, J. Ko, V. Saravanan, S. Lee, Stochastic analysis of a single-rotor to quantify the effect of RPS variation on noise of hovering multirotors, Appl. Acoust. 182 (2021), 108224, https://doi.org/10.1016/j.apacoust.2021.108224.
[16] M.B.S. Magalhaes, R.A. Tenenbaum, Sound sources reconstruction techniques: a review of their evolution and new trends, Acta. Acust. united Ac. 90 (2004) 199–220, https://doi.org/10.1134/1.1675880.
[17] P. Chiariotti, M. Martarelli, P. Castellini, Acoustic beamforming for noise source localization – reviews, methodology and applications, Mech. Syst. Signal Process. 120 (2019) 422–448, https://doi.org/10.1016/j.ymssp.2018.09.019.
[18] C.C. Pagani, D.S. Souza, M. Medeiros, Slat noise: aeroacoustic beamforming in closed-section wind tunnel with numerical comparison, AIAA J. (2016) 1–16, https://doi.org/10.2514/1.J054042.
[19] T.V. Wood, S.M. Grace, Inverse aeroacoustic problem for a rectangular wing, AIAA J. 38 (2000) 203–210, https://doi.org/10.2514/2.963.
[20] T. Suzuki, L1 generalized inverse beamforming algorithm resolving coherent/incoherent, distributed and multipole sources, J. Sound Vib. 330 (2013) 5835–5851, https://doi.org/10.1016/j.jsv.2011.05.021.
[21] H.S. Kwon, Y. Niu, Y.J. Kim, Planar nearfield acoustical holography in moving fluid medium at subsonic and uniform velocitya, J. Acoust. Soc. Am. 128 (2010) 1823–1832, https://doi.org/10.1121/1.3478771.
[22] B.C. Dong, C.X. Bi, X.Z. Zhang, Y.B. Zhang, Real-time nearfield acoustic holography in a uniformly moving medium, J. Sound Vib. 410 (2017) 364–377, https://doi.org/10.1016/j.jsv.2017.08.040.
[23] S. Ianniello, The Ffowcs Williams–Hawkings equation for hydroacoustic analysis of rotating blades. Part 1. the rotpole, J. Fluid Mech. 797 (2016) 345–388, https://doi.org/10.1017/jfm.2016.263.
[24] B. Barsikow, W. Iii, On removing the Doppler frequency shift from array measurements of railway noise, J. Sound Vib. 120 (1988) 190–196, https://doi.org/10.1016/0022-460X(88)90344-6.
[25] H.P. Verhas, A restoration procedure for (non-stationary) signals from moving sources, J. Sound Vib. 89 (1983) 487–497, https://doi.org/10.1016/0022-460X(83)90350-4.
[26] X.Z. Zhang, C.X. Bi, Y.B. Zhang, L. Xu, A time-domain inverse technique for the localization and quantification of rotating sound sources, Mech. Syst. Signal Process. 90 (2017) 15–29, https://doi.org/10.1016/j.ymssp.2016.12.003.
[27] X.J. Pan, H.J. Wu, W.K. Jiang, Beamforming correction for the singular problem in identifying rotating sources with non-uniform directivity, J. Acoust. Soc. Am. 147 (2020) 3151–3159, https://doi.org/10.1121/10.0001169.
[28] W. Ma, H. Bao, C. Zhang, X. Liu, Beamforming of phased microphone array for rotating sound source localization, J. Sound Vib. 467 (2020), 115064, https://doi.org/10.1016/j.jsv.2019.115064.
[29] C.X. Bi, Y. Xu, Y.B. Zhang, et al., A time-domain inverse method for the localization and quantification of unsteady rotating loading sources, J. Sound Vib. 512 (2021), 116405, https://doi.org/10.1016/j.jsv.2021.116405.
[30] P. Sijtsma, S. Oerlemans, H. Holthusen, Location of rotating sources by phased array measurements, in: Proceedings of the 25th 7th AIAA/CEAS Aeroacoustic Conference, 2001, https://doi.org/10.2514/6.2001-2167, 2001–2167.
[31] R.P. Dougherty, B. Walker, Virtual rotating microphone imaging of broadband fan noise, in: Proceedings of the 25th AIAA/CEAS Aeroacoustics Conference, 2009, https://doi.org/10.2514/6.2009-3121.
[32] W. Pannert, C. Maier, Rotating beamforming-motion-compensation in the frequency domain and application of high-resolution beamforming algorithms, J. Sound Vib. 333 (2014) 1899–1922, https://doi.org/10.1016/j.jsv.2013.11.031.
[33] P. Sijtsma, Using phased array beamforming to identify broadband noise sources in a turbofan engine, Int. J. Aeroacoust. 9 (2010) 357–374, https://doi.org/10.1260/1475-472X.9.3.357.
[34] S. Oerlemans, P. Sijtsma, B.M. López, Location and quantification of noise sources on a wind turbine, J. Sound Vib. 299 (2007) 869–883, https://doi.org/10.1016/j.jsv.2006.07.032.
[35] C. Ocker, W. Pannert, Imaging of broadband noise from rotating sources in uniform axial flow, AIAA J. 55 (2016) 1185–1193, https://doi.org/10.2514/1.J055309.
[36] L. Yu, H. Wu, J. Antoni, W. Jiang, Extraction and imaging of aerodynamically generated sound field of rotor blades in the wind tunnel test, Mech. Syst. Signal Process. 116 (2019) 1017–1028, https://doi.org/10.1016/j.ymssp.2018.07.042.
[37] S.E. Wright, Sound radiation from a lifting rotor generated by asymmetric disk loading, J. Sound Vib. 9 (1969) 223–240, https://doi.org/10.1016/0022-460X(69)90029-7.
[38] S. Glegg, W. Devenport, Aeroacoustics of Low Mach Number Flows: Fundamentals, Analysis, and Measurement, Academic Press, London, United Kingdom, 2017.
[39] W.Q. Chen, B. Peng, R.P. Liem, X. Huang, Experimental study of airfoil-rotor interaction noise by wavelet beamforming, J. Acoust. Soc. Am. 147 (2020) 3248–3259, https://doi.org/10.1121/10.0001209.
[40] A. Gérard, A. Berry, P. Masson, Control of tonal noise from subsonic axial fan. Part 1: reconstruction of aeroacoustic sources from far-field sound pressure, J. Sound Vib. 288 (2005) 1049–1075, https://doi.org/10.1016/j.jsv.2005.01.023.
[41] H. Trabelsi, M. Abid, M. Taktak, T. Fakhfakh, M. Haddar, Reconstruction of the unsteady rotating forces of fan's blade from far-field sound pressure, Appl. Acoust. 86 (2014) 126–137, https://doi.org/10.1016/j.apacoust.2014.03.008.
[42] C.R. Lowis, P.F. Joseph, Determining the strength of rotating broadband sources in ducts by inverse methods, J. Sound Vib. 295 (2006) 614–632, https://doi.org/10.1016/j.jsv.2006.01.031.
[43] A. Najafi-Yazdi, G.A. Brès, L. Mongeau, An acoustic analogy formulation for moving sources in uniformly moving media, Proc. Roy. Soc. A Math. Phys. 461 (2011) 2125, https://doi.org/10.1098/rspa.2010.0172.
[44] S. Lee, K.S. Brentner, P.J. Morris, Acoustic scattering in the time domain using an equivalent source method, AIAA J. 48 (2010) 2772–2780, https://doi.org/10.2514/1.45132.
[45] S. Lee, K.S. Brentner, P.J. Morris, Assessment of time-domain equivalent source method for acoustic scattering, AIAA J. 49 (2011) 1897–1906, https://doi.org/10.2514/1.J050736.
[46] P.A. Nelson, S.H. Yoon, Estimation of acoustic source strength by inverse methods: part I, conditioning of the inverse problem, J. Sound. Vib. 233 (2000) 643–668, https://doi.org/10.1006/jsvi.1999.2837.
[47] S.H. Yoon, P.A. Nelson, Estimation of acoustic source strength by inverse methods: part II, experimental investigation of methods for choosing regularization parameters, J. Sound. Vib. 233 (2000) 669–705, https://doi.org/10.1006/jsvi.2000.2836.

[48] A. Kazemi Amiri, C. Bucher, Derivation of a new parametric impulse response matrix utilized for nodal wind load identification by response measurement, J. Sound Vib. 344 (2015) 101–113, https://doi.org/10.1016/j.jsv.2014.12.027.
[49] B. Qiao, X. Zhang, C. Wang, H. Zhang, X. Chen, Sparse regularization for force identification using dictionaries, J. Sound Vib. (2016) 71–86, https://doi.org/10.1016/j.jsv.2016.04.040.
[50] M. Aucejo, O. De Smet, A novel algorithm for solving multiplicative mixed-norm regularization problems, Mech. Syst. Signal Process. 144 (2020), 106887, https://doi.org/10.1016/j.ymssp.2020.106887.
[51] A. Gramfort, M. Kowalski, M. Hamalainen, Mixed-norm estimates for the m/eeg inverse problem using accelerated gradient methods, Phys. Med. Biol. 57 (2012) 1937–1961, https://doi.org/10.1088/0031-9155/57/7/1937.
[52] M. Aucejo, O. De Smet, Bayesian source identification using local priors, Mech. Syst. Signal Process. 66/67 (2016) 120–136, https://doi.org/10.1016/j.ymssp.2015.05.004.
[53] P.C. Hansen, D.P.O. Leary, The use of the L-curve in the regularization of discrete ill-posed problems, SIAM J. Sci. Comput. 14 (1993) 1487–1503, https://doi.org/10.1137/0914086.
[54] S. Paillasseur, J.H. Thomas, J.C. Pascal, Regularization for improving the deconvolution in real-time near-field acoustic holography, J. Acoust. Soc. Am. 129 (2011) 3777–3787, https://doi.org/10.1121/1.3586790.